Additive Manufacturing 75 (2023) 103736

Contents lists available at ScienceDirect

Additive Manufacturing

journal homepage: www.elsevier.com/locate/addma

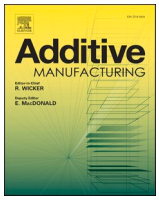

Deformations modelling of metal additively manufactured parts and improved comparison of in-process monitoring and post-process X-ray computed tomography

Nicolò Bonato *, Filippo Zanini, Simone Carmignato

Department of Management and Engineering, University of Padua, Vicenza, Italy

ARTICLE INFO

Keywords:
Laser powder bed fusion
In-process monitoring
X-ray computed tomography
Data alignment
Process modelling

ABSTRACT

The comparison of potential defects detected through in-process real-time monitoring systems and actual defects measured in the fabricated parts by X-ray computed tomography offers relevant opportunities for improving the understanding, sustainability and precision of metal laser powder bed fusion processes. However, the comparison outcome strongly depends on data alignment accuracy, which is hindered by typical process-induced part deformations arising during and after production. This work presents a methodology that includes the modelling of part deformations for improving the alignment and comparison of in-process and post-process datasets. The methodology was successfully implemented, starting from deformations predicted by process simulations, and verified experimentally by producing samples including fiducials specifically designed to provide insights on local deformations. Results show an improved data alignment accuracy, which is fundamental for enabling the establishment of robust correlations aiding the reduction of false positives and false negatives in the in-process gathered signals. The approach is also found to be effective in accurately categorizing non-significant process signatures occurring during the fabrication, hence preventing the implementation of wrong corrective actions.

1. Introduction

Additive manufacturing (AM) technologies, and particularly laser-based powder bed fusion (PBF-LB/M) of metals, are increasingly adopted to fabricate high-value-added parts for applications in different industries, including biomedical, aerospace, automotive, tooling and consumer goods [1]. However, the stringent quality standards requested in several applications are still challenging, while PBF-LB/M metal parts can present various types of flaws undermining product functionality or service life.

In particular, internal porosities – taking place in PBF-LB/M parts depending on the process conditions [2] – were demonstrated to have a significant impact on mechanical properties [3]. Despite several attempts to optimize the process parameters, parts fabricated by PBF-LB/M still manifest variable mechanical properties due to difficult-to-predict defects, whose specific causes are not always comprehensively understood yet [4]. Lack-of-fusion voids, which can be easily distinguished from gas and keyhole pores for the relevant size, the characteristic irregular shape and the presence of partly melted entrapped powder particles, highly affect part resistance, with fatigue failures frequently initiating at the material-pore interface [5]. Since the exact reasons behind lack-of-fusion pores' formation are still not always clear, recent works started investigating this aspect to increase the experimental knowledge on the relationship between PBF-LB/M process anomalies and actual part defects. For example, Snow et al. [6] recently found a statistically significant causal relationship between spatter particles (i.e., particles ejected from the melt pool and dropping onto the powder bed) and lack-of-fusion voids by using in-situ process monitoring. In addition to this example, in-situ and on-machine process monitoring solutions have been increasingly employed in recent years to gather useful information about process intrinsic dynamics and to move towards first-time-right sustainable manufacturing [7]. The iterative layer-wise nature of AM processes is indeed well suited to the integration of sensors for monitoring the fabrication while it is ongoing [8], providing valuable knowledge regarding defects formation at their early onset stage, thus paving the way to the complete process automation and real-time defects healing by acting on the process under a closed-loop control [9]. Robust process control can also reduce wastes, the need for time-consuming and expensive post-process analyses and finishing operations, and mechanical properties variability.

* Correspondence to: Stradella San Nicola 3, 36100 Vicenza, Italy.
E-mail address: nicolo.bonato@phd.unipd.it (N. Bonato).

https://doi.org/10.1016/j.addma.2023.103736
Received 7 April 2023; Received in revised form 3 July 2023; Accepted 10 August 2023
Available online 11 August 2023

Several studies have been conducted regarding PBF-LB/M in-process monitoring (see for example the works by Coeck et al. [10], Zouhri et al. [11] and Caggiano et al. [12]), testing different solutions in terms of sensors integration and types of gathered data. An important stream of research deals with the analysis of high-resolution images of the entire layer [13], mainly acquired in the visible [14] and the near-infrared [15] wavelength range. Other sensors are more focused towards catching the process dynamics by acquiring data such as high-speed melt pool images [16], pyrometric signals [17] or by registering acoustic emissions [18]. A huge amount of information is obtained from each build-job, which implies the need to properly manage and process the acquired data. In this context, machine learning and deep learning algorithms have been vastly applied because of the chance to learn unknown relations without the need for developing highly-complex analytical models (see for example the works by Baumgartl et al. [19], Snow et al. [20] and Scime et al. [21]). Although the undeniable advantages, such as the opportunity of a continuous model re-training on new data, the capability of real-time feature extraction and anomaly classification [7], these algorithms may be lacking physical interpretability [22].

Obtaining a reliable ground truth dataset regarding actual flaws to be related to process anomalies observed during the process is therefore of utmost importance. In this context, X-ray computed tomography (CT) has the ability to provide comprehensive information about both external and internal geometry and defects [23]. Hence, it can be employed to perform post-process measurements of PBF-LB/M parts and generate reference data for validating process monitoring solutions.

A current main challenge is related to the fact that not all the anomalies observed from in-process monitoring correspond to actual defects of the fabricated part. Two possible causes are: (i) some anomalies arising in the current layer might be “cured” when generating the subsequent ones [24]; (ii) the accuracy of the alignment between in-process and post-process acquired data can be hindered by deformations occurring during and/or after the PBF-LB/M fabrication [25]. While in-process data are acquired during the process on planes whose normal vectors are parallel to the building direction, post-process CT data are obtained after the fabrication when the corresponding cross-sections might lie on planes with modified positions and orientations due to part deformations. However, cross-sections extracted from CT reconstructions are commonly directly compared with layer-wise in-process acquisitions at their nominal height positions, using simple sample geometries, such as cylinders or cubes (see for example Mohr et al. [15]), which do not include geometrical features suited to perform accurate data alignment and comparison. The need to integrate into the produced parts adequate reference fiducials for the alignment of acquired data was highlighted in [25], where some initial design guidelines were provided. An alternative approach dealing with data alignment can be found in the work by Oster et al. [26], with particular focus on non-planar layers deformations. Such deformations were locally described by studying the transition surface between regions fabricated with significantly different process parameters; however, linear interpolations were assumed for approximating the deformations of all the other layers included within each region.

Nevertheless, comprehensive methods to design proper parts geometries and procedures to conduct accurate alignments between in-process and post-process data taking into account process-induced part deformations are still missing. This work aims at addressing the aforementioned research gap, by developing a methodology enabling the effective alignment and comparison between in-process monitoring data and CT post-process measurements. First, an analytical approach is proposed to model the deformations affecting the fabricated sample. Second, the number of reference fiducials and corresponding reference points needed on the part to implement the approach and generate the model is investigated using PBF-LB/M process simulations and considering the influence of the measurement uncertainty. The obtained model is then used to design suited sample geometries including the adequate number of reference fiducials. Manufacturing and metrology requirements are taken into account in the sample design. The method is finally implemented and verified experimentally.

2. Method to model AM part deformations

Fig. 1 shows a schematic representation of a deformed cylindrical sample with the presence of an internal defect. The cross-section parallel to the cylinder base taken at a z-position where the in-process monitoring showed an anomaly (red section in Fig. 1a) does not include the related defect because this position does not take into account the final part deformation. The actual section plane crossing the defect (yellow section in Fig. 1b) can be identified by three points belonging to the after-build plane. Due to the CT measurement uncertainty, represented as an ellipsoid around each point (see Fig. 1c), the measured cross-section plane (see the blue section in Fig. 1c) can differ from the actual one. In this case, the capability to cross and detect the defect depends on both the defect size and the measurement uncertainty. Fig. 1 also highlights the fact that a bad alignment between datasets increases the number of false positive and false negative signals detected comparing the datasets.

2.1. Proposed modelling approach

The methodology proposed in this work to model the PBF-LB/M part deformations/deviations is schematized in Fig. 2. The main goal is to apply an analytical model for describing the deformations of interest for aligning the datasets. The starting point to implement the methodology is constituted by describing part deformations, such as a priori knowledge from literature, experiments or numerical simulations. In this work, such data are specifically obtained through simulations performed on cylindrical samples using the commercial software ANSYS (ANSYS, Inc, US). Shape and dimensions have been chosen to allow for post-process CT scans with high resolution, while still providing a representative material volume for defects analysis [25,27]. The deviations caused by the simulated part deformations are extracted along each axis of the coordinate reference system (namely, δx, δy, δz) for a number of reference points placed on the surface of cylindrical samples. Specifically, the reference points are arranged on a number of different z-levels, i.e., along the building direction, and grouped in three per level to generate a plane (as the one in Fig. 1b) defining the position and orientation of the produced layer. Deviations δx, δy, and δz are then treated as the response variable of a two-variable polynomial regression, defined as per Equation (1),

$$\begin{cases} \delta x = f_1(z, \alpha) \\ \delta y = f_2(z, \alpha) \\ \delta z = f_3(z, \alpha) \end{cases} \tag{1}$$

where the selected input variables are the nominal z value,

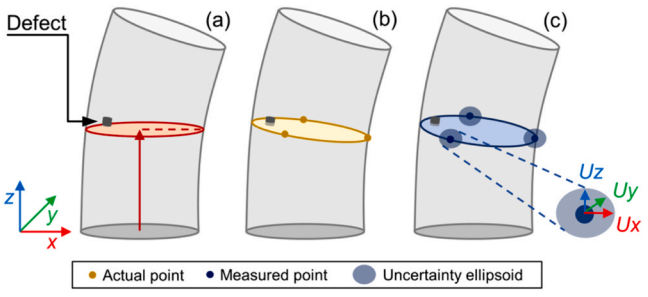

Fig. 1. Schematic representation of a deformed cylinder including an internal defect, with nominal cross-section parallel to the cylinder base (a), actual cross-section intersecting the defect (b), and measured cross-section with points uncertainty represented as surrounding ellipsoids (c).

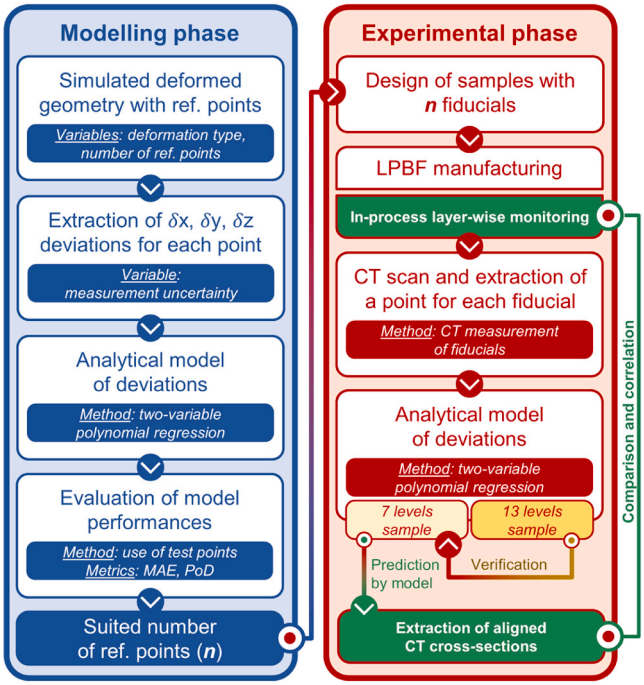

Fig. 2. Schematic representation of the proposed methodology workflow.

representative of possible deviations along the building direction, and the nominal angle α in the x-y plane, representative of possible cross-section tilting. Such variables are then scaled through feature standardization and a statistical significance analysis is performed to select the adequate grade for each variable before implementing the polynomial regression, resulting in a highest grade of two and three for z and α, respectively. The models obtained from the reference points can then be used to predict the deviations of other points on the surface of the samples (i.e., test points) and the position of cross-sectional planes. The position of the test points and of cross-sectional planes on the deformed part is known from simulations, hence prediction errors can be quantified using the metrics described in Section 2.2. The number of reference points used for the modelling phase influences the magnitude of prediction errors. Consequently, the suited number of reference points has to be defined. This will determine the number of reference fiducials needed in the design of samples to be manufactured for experimental implementation and verification of the proposed methodology. Different numbers of reference points were hence investigated, and two specific cases are taken as examples in the following. The first case consists of 7 z-levels (equally spaced by 1.4 mm along the z-axis) used for generating the model, plus 6 intermediate z-levels used for testing the obtained model. The second case, instead, consists of 14 z-levels (equally spaced by 0.7 mm along the z-axis) used for the modelling phase, plus 13 intermediate z-levels used for the testing phase. Each level is characterized by three reference/test points, for a total of 39 and 81 points in the two cases, respectively.

Different uncertainty values were also tested by considering the measurement uncertainty contribution as an ellipsoid surrounding the reference points measured for the modelling phase. For each tested uncertainty value, the coordinates of these points were recalculated within the defined ellipsoid using a three-dimensional (3D) Gaussian probability distribution.

After testing the effect of different numbers of reference points used for modelling the deformed part geometry, including also the influence of the type of deformation and the measurement uncertainty, the required number of reference fiducials is then determined. This number is then used to drive the design of an appropriate task-specific geometry to be used in the experimental phase, including PBF-LB/M manufacturing and in-process monitoring, as reported in Fig. 2 and explained in Section 3.

2.2. Effect of number of levels and measurement uncertainty

The combined effect of the number of reference points/levels and the measurement uncertainty is investigated using two metrics: the mean absolute error (MAE) to quantify deviations between predicted and actual test point coordinates in the deformed sample, and the probability of detection (PoD) of defects to calculate the probability of one predicted plane to cross/detect a defect of a certain dimension inside the sample. The second metric is particularly important because, for in-process monitoring, what matters the most is to enable the detection of the appropriate layer within the manufactured sample (i.e., within the reconstructed CT volume), in order to accurately compare it with the corresponding layer-wise data acquired during the fabrication. Fig. 3a shows the MAE values obtained for the two addressed cases with 7 and 14 levels of fiducials, respectively, for the case of uniform measurement uncertainty (same expanded uncertainty, U, in the three directions: $Ux = Uy = Uz$). An increasing trend of MAE with respect to the measurement uncertainty is observed, with lower values and a slower increase when more levels are used for the modelling phase. Moreover, in both cases, MAEs are higher for the z-direction.

Fig. 3b illustrates the PoD values related to different defect dimensions (cylindrical defects with height-to-diameter ratio equal to 1 were considered), number of levels and uncertainties. The PoD was calculated by varying the uncertainty contribution related to the reference points used in the modelling phase so that the predicted plane differs from the actual plane in terms of position and orientation. A defect of a certain dimension and located on a particular position within

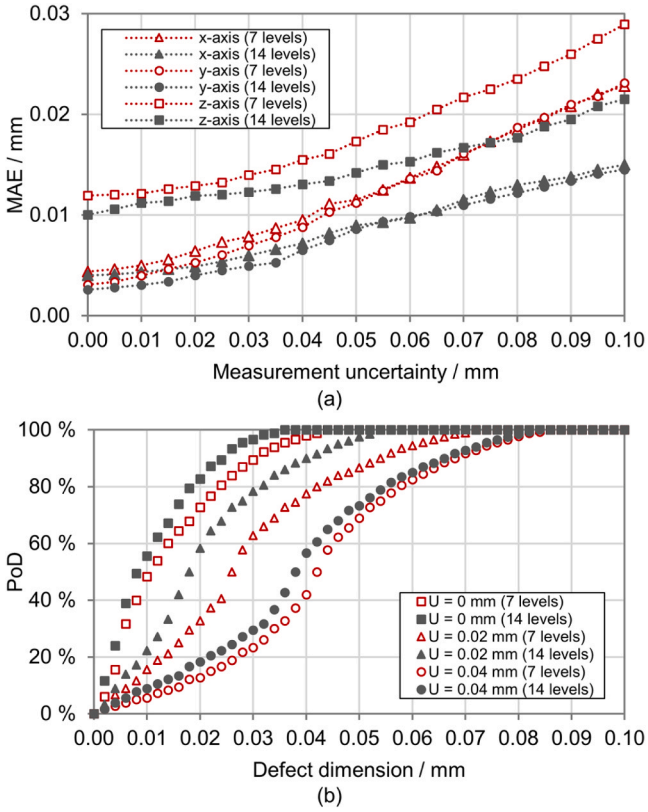

Fig. 3. Mean absolute error (MAE) against measurement uncertainty, for the cases with 7 and 14 levels used for the modelling phase (a). Probability of detection (PoD) against defect dimension, for the two cases with 7 and 14 training levels grouped by three different values of CT measurement uncertainty: 0, 0.02, 0.04 mm (b).

a layer was considered detected when crossed by the predicted plane. Fig. 3b shows that the defects detectable with a good probability (e.g., 90%) increase in dimension when the measurement uncertainty increases. Moreover, the probability of detecting a defect of a certain dimension becomes higher when using a sample with a higher number of levels of fiducials. For a quantitative perspective, we direct the reader to the values reported in Fig. 3b.

3. Implementation and verification of the methodology

Section 3.1 presents the sample design, which includes the integration of fiducials for measuring reference points within the fabricated samples. An additional sample design is also presented to provide experimental validation of the modelling methodology. The PBF-LB/M monitoring setup and the in-process gathered data are described in Section 3.2, where the CT post-process analyses are documented as well. Measurements performed after CT reconstruction are finally addressed in Section 3.3.

3.1. Design of part geometries and reference fiducials

In order to experimentally implement and verify the methodology described in Section 2, two different part geometries were designed: one with 7 levels of fiducials (Fig. 4a), and another with 13 levels of fiducials (Fig. 4b). Reference fiducials are included to derive reference points as described in Section 3.3. Reference points retrieved on the geometry with 7 levels are used to model specific deformations affecting the part, while the geometry with 13 levels serves as experimental verification of the methodology. In fact, in the part with 13 levels, 7 levels are used for the modelling phase and the other 6 intermediate levels for the testing phase.

Starting from a preliminary study [27], design for additive manufacturing [28] and design for metrology [29] guidelines were both taken into account. In particular, (i) an overall cylindrical shape with a diameter of 9 mm and height of 10 mm was chosen to enable high-resolution CT scans, needed to measure micro-scale defects; (ii) the fiducials were designed as pockets characterized by a base plane (horizontal plane) superimposed by a cylinder (diameter 1.2 mm; height 1.3 mm) as shown in Fig. 4. For improving the least-squares fitting of geometrical elements, base planes are smoothed by re-melting during the PBF-LB/M process, while cylinders are built parallel to the building direction to obtain a more homogeneous surface texture and reduced form errors. Moreover, cylinders are partially submerged into the main shape to be subjected to the same deformations affecting the entire part. Three equally spaced fiducials were arranged in each level to obtain three reference points and a plane to be used either for the modelling phase (using 7 levels in both geometries) or for the testing phase (using the additional intermediate 6 levels in the second geometry). A cylindrical base with a height equal to 2 mm was also added to aid a first rough alignment by exploiting the integration of a notch, which locks all the spatial degrees of freedom.

It is worth mentioning that different overall dimensions of samples and designs of fiducials were tested before finding an adequate solution with the final proposed geometry illustrated in Fig. 4. For example, fiducials composed of spheres and tilted cylinders were found to be more affected by form errors and non-homogeneous surface texture, full vertical cylinders not submerged into the main shape were observed to be subjected to specific local deviations, and smaller sizes led to build quality issues for the fiducials.

3.2. PBF-LB/M, monitoring setup and CT post-process analyses

Specimens with the proposed geometries were fabricated using a PBF-LB/M machine, Sisma MYSINT100 (Sisma SpA, Italy), and a titanium alloy, Ti6Al4V. The parts shown in Fig. 5a were manufactured with a laser power of 155 W, scanning speed of 1200 mm/s, hatch spacing of 110 μm, and layer thickness of 20 μm. The laser power was reduced by 50% for down-facing surfaces to reduce the dross formation [30].

An off-axis in-process monitoring setup featuring a high-resolution Digital Single-Lens Reflex (DSLR) was used to acquire long-exposure images to detect hot spot signals caused by the undesired presence of spatter particles above the powder bed, which can hamper the complete melting of powder [31]. Images acquired with this technique are reported in Fig. 8c and f as examples.

A metrological micro-CT system (Nikon Metrology MCT225) was used to scan the samples, with tube voltage equal to 200 kV, current equal to 35 μA, 2000 projections, and exposure time of 1420 ms. A 0.1 mm copper filter was used to reduce beam hardening. A voxel size equal to 7.7 μm was achieved. The acquired projections were employed for reconstructing the 3D volume of the samples (see examples in Fig. 5b-top and Fig. 5b-bottom). Then, a local-adaptive surface determination was performed using VGStudio Max 3.2 (Volume Graphics, GmbH).

3.3. Data alignment and reference points measurement

For each fiducial, least-squares fitting of plane and cylinder were conducted in VGStudio Max 3.2. The axis of the cylinder was intersected with the corresponding base plane to obtain a reference point. By repeating this procedure for all the fiducials, a total of 7 and 13 triplets of points (each defining a local plane) were obtained for the two different geometries. As per the methodology in Section 2, the obtained points are used to feed the two-variable polynomial regression, enabling the prediction of both position and orientation of any layer within the CT volume. In accordance with Section 3.1, the sample with 13 levels serves as an experimental validation of the sample with 7 levels. In fact, 7 of the 13 levels are used for the modelling phase, while the remaining

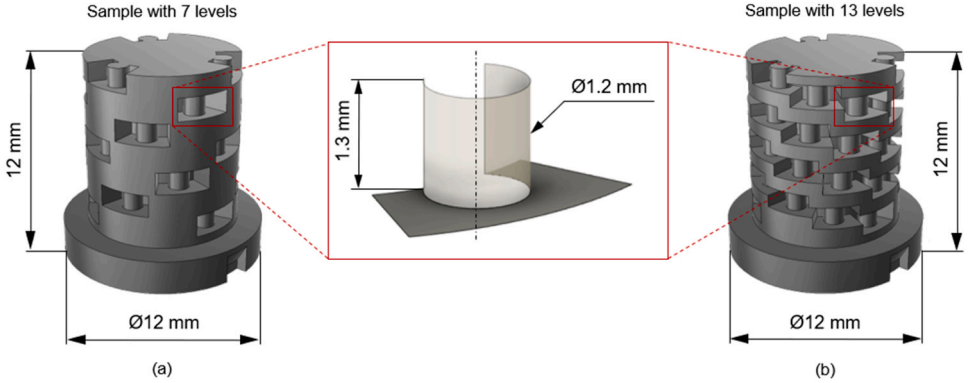

Fig. 4. Design of samples including 21 fiducials arranged on 7 levels (a), and 39 fiducials on 13 levels (b).

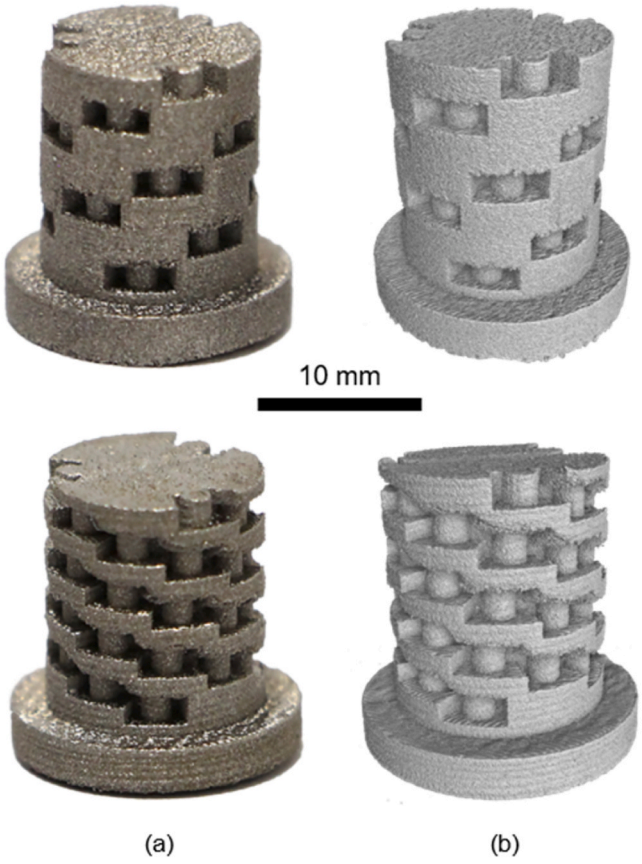

Fig. 5. Fabricated parts (a) and corresponding CT reconstructed geometries (b), with 7 (top) and 13 levels (bottom).

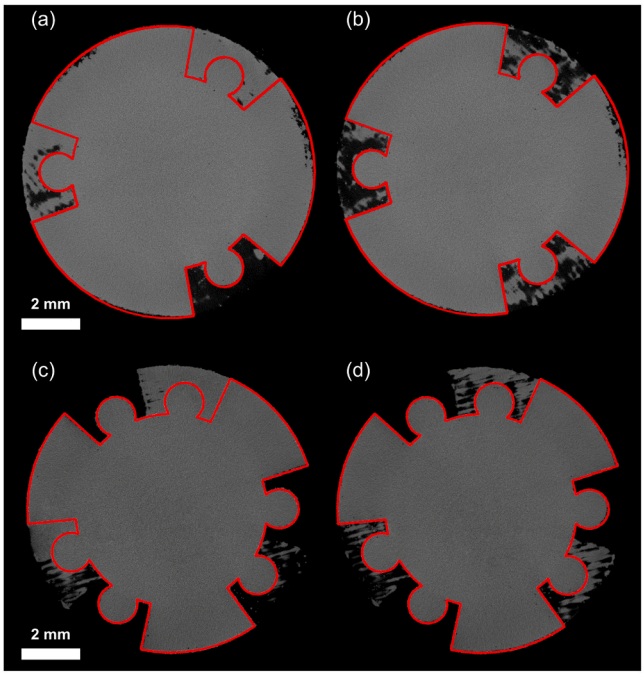

Fig. 6. Comparison between the nominal contour (in red) and the corresponding CT cross-section extracted with conventional alignment (a, c) and with the newly proposed alignment method (b, d). The comparison is shown for both a reference level of a sample with 7 levels (a, b) and a testing level of a sample with 13 levels (c, d).

6 levels constitute the testing set in which the MAEs are evaluated.

4. Experimental results

This paragraph describes the experimental results obtained on real fabricated samples. The errors evaluation and the comparison between conventional and newly developed alignment methods are reported in Section 4.1, while Section 4.2 highlights the potential of the presented method for improving the comparison accuracy between in-process monitoring and post-process CT datasets.

4.1. Errors evaluation and comparison with standard alignment

Experiments conducted on the sample with 13 levels resulted in MAEs equal to 8, 7 and 14 μm, respectively for the x, y and z directions. The trend obtained for these errors is coherent with the simulations results reported in Section 2.2. The magnitude of the registered MAEs is compatible with a typical target of detecting porosities with a size of tens of micrometres in PBF-LB/M parts, such as lack-of-fusion defects caused by spatters [6]. Therefore, for this target, the sample with 7 levels of fiducials can be used for generating the part deformation model to be employed for the prediction of effective after-build layers' position and orientation.

Fig. 6a shows the superimposition of the contour obtained from one nominal section of interest of such sample to the corresponding CT cross-section extracted by means of a conventional alignment (i.e., using a cutting plane parallel to the platform), which is far different with respect to the nominal section of interest. In Fig. 6b the proposed alignment using reference fiducials is used to obtain an improved cross-section extraction, much closer to the section of interest. Such improved cross-section is related to a reference level to demonstrate that the integrated fiducials provide adequate reference points for the alignment improvement. In addition, a similar comparison conducted on a testing level of the sample with 13 levels is reported in Fig. 6c and d. Fig. 6c shows the superimposition of the nominal contour with the corresponding CT cross-section obtained through the conventional alignment. Fig. 6d represents instead improved comparison between the nominal contour and the CT cross-section obtained by means of model predictions on the testing level. Also in this case the predicted cross-section is much closer to the nominal contour with respect to the one obtained with the conventional alignment, which does not take into account the local deformation.

A quantitative comparison between the conventional and the newly proposed alignment is also reported in Fig. 7 for two examples of reference levels taken at different heights along the building direction. The light-blue horizontal planes are referred to the conventional alignment, while the coloured planes are obtained by means of the three reference points provided by the fiducials.

As can be seen, the planes determined by using the reference points are shifted and tilted with respect to the planes obtained by conventional alignment. The presented modelling methodology can be exploited by performing a re-slicing of the entire CT volume based on each predicted cross-sectional plane.

4.2. Improvement of comparison between monitoring and CT data

The alignment methodology proposed in this work was finally implemented to improve the comparison between in-process layer-wise data and related CT cross-sections. A couple of examples related to defects detected from CT scans in two different layers are shown in Fig. 8.

Fig. 8(a, d) and (b, e) represent the CT cross-sections obtained through the conventional alignment and through the predicted aligned plane, respectively. As explained in Section 2.1, the extraction of the improved aligned CT cross-section plane is obtained through the prediction of three points carried out by means of the trained model.

Fig. 8(c, f) shows the corresponding long-exposure images acquired

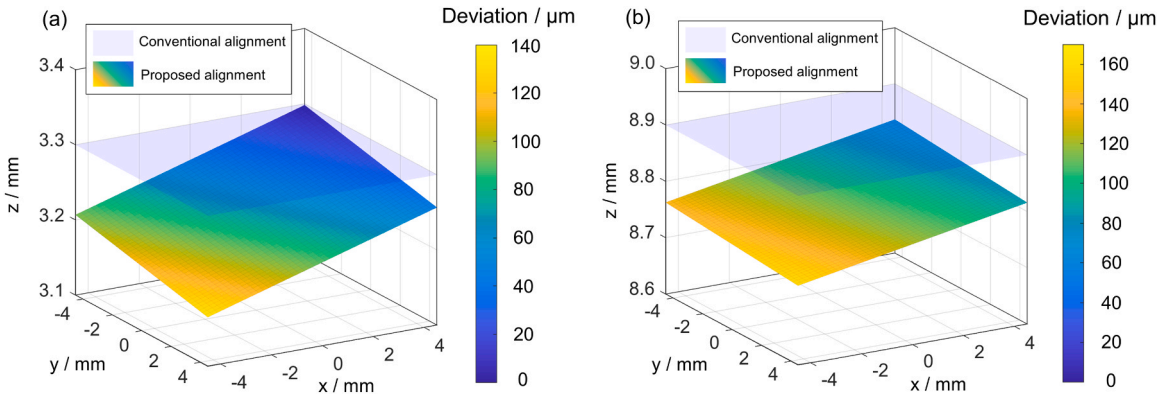

Fig. 7. Deviations between conventional and proposed alignment represented by visualizing the two different cross-section planes for the third (a) and the seventh (b) level of a sample with 7 reference levels.

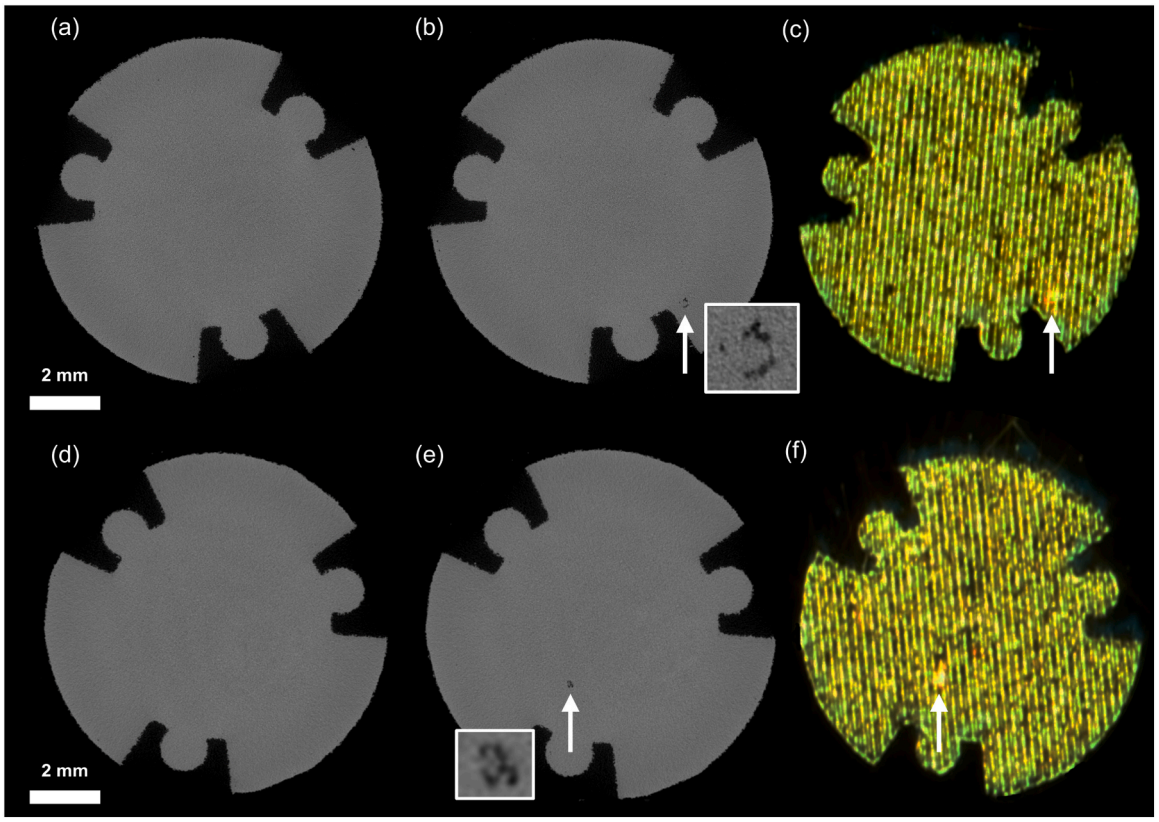

Fig. 8. Comparison of post-process and in-process data in the case of two defects detected in different layers: CT slices obtained with conventional alignment (a, d) and proposed alignment (resulting from model predictions) showing a defect (b, e), and corresponding in-process long-exposure images showing an anomaly (c, f).

during the PBF-LB/M process, where a hot spot is visible (indicated by the white arrow). While the conventional alignment was not successful in detecting the defect caused by such hot spot, the cross-section determined with the proposed alignment methodology successfully revealed the presence of a lack-of-fusion pore in the hot spot regions. Furthermore, each defect is surrounding a solid round particle (as shown in the insets of Fig. 8b and e), which indicates a clear link with a spatter particle that dropped onto that specific zone within the layer, hence enabling the identification of the cause of the defect. This behaviour was observed also on other defects caused by spatters within the same sample as well as on other samples that were manufactured and analysed during this research. It is worth highlighting that the in-process long-exposure images of Fig. 8(c, f) show also a number of dark regions caused by a non-uniform action of the laser over the processed powder layer. However, such regions do not find any correspondence with actual lack-of-fusions defects in the CT reconstructed volume. This means that the potential lack-of-fusion regions are eventually cured by the energy provided by the laser in the following layers. The confidence in the results and the implications discussed in this section is possible only thanks to the accurate alignment between in-process and post-process data enabled by the methodology proposed in this work. Such methodology can hence be used to accurately correlate process anomalies with actual defects to improve the process knowledge as well as to move forward an effective analysis and use of in-process gathered signals. For example, these signals can be elaborated to obtain metrics to predict the final part quality and to take automatic reliable decisions and active actions during the process itself. Furthermore, even if in this work the methodology was specifically tested on optical layer-wise

acquisitions, it can be certainly extended to different in-process monitoring techniques.

5. Conclusions

This work addressed the challenge related to the alignment and comparison of PBF-LB/M in-process monitoring data and post-process CT measurements, which are needed to better understand the PBF-LB/M process and improve its precision and sustainability. In particular, a new methodology was proposed to model the geometry of samples specifically designed for PBF-LB/M in-process monitoring, including their distortions, to identify the actual position and orientation taken on after the process by cross-sections that were previously analysed by in-process techniques. A two-variable polynomial regression was determined effective for the modelling task. The suited number of reference fiducials to be included in the designed parts was investigated analytically by evaluating the performances of the model for different CT measurement uncertainties and different dimensions of possible defects of interest. Based on the results of the analysis, showing that a sample with 7 fiducials levels was suited for detecting the defects of interest, adequate geometries and reference fiducials were designed by considering the requirements of PBF-LB/M manufacturing as well as of CT metrology. Samples were then produced by PBF-LB/M and monitored during the process by long-exposure imaging to apply the modelling procedure to actual parts and provide experimental validation of the methodology proposed in this research.

The errors (MAEs) of the reference points positions within the entire part predicted by the generated model were determined to be below 14 μm for all the axial directions. These values are small enough to ensure the detection of pores with dimensions above 50 μm (typical minimum size of lack-of-fusion pores caused by spatter particles in the PBF-LB/M parts investigated in this work) with a probability of detection above 90% considering the model trained on 7 reference levels and a measurement uncertainty equal to 20 μm (deliberately higher than the uncertainty obtainable when measuring internal pores with the CT system used in this work, as shown in [32]). Results demonstrated that the methodology proposed in this work leads to a higher alignment accuracy and to an improved comparison between in-process detected anomalies and CT-measured actual defects, thus enabling the establishment of robust correlations through the reduction of both false positives and false negatives.

In addition, the datasets collected during the PBF-LB/M manufacturing process have revealed a significant presence of dark spots that did not lead to any defect with a size equal to or larger than 50 μm (which corresponds to a size value that was determined relevant for cracks initiation in cyclically loaded Ti6Al4V PBF-LB/M samples [33, 34]). Despite these spots have to be discerned as insignificant events (or false positives) occurring during the interaction between the laser and the powder, they could potentially be classified as relevant signals if not compared with well-aligned post-process tomographic data. Consequently, it can be concluded that the ground truth obtained from the extracted CT slices, when appropriately aligned, is crucial to accurately categorize these events and to avoid the implementation of wrong corrective actions. The developed methodology will be exploited in future works also to enhance the accuracy of advanced algorithms for analysing in-process datasets, such as machine learning and deep learning models for real-time defect classification or segmentation. Given the complexity of some of these models, which often leads to a lack of interpretability in their results, an accurate ground truth such as that provided by the presented workflow is essential in avoiding biased or even unreliable outcomes.

Future developments of this research will focus on enhancing the presented non-linear modelling approach by considering non-planar layers deformations that contribute to data alignment and comparison as highlighted in [26]. The methodology can now be used with the proposed sample geometry for improving and validating different in-process PBF-LB/M monitoring solutions employing various sensors through accurate comparison with appropriately aligned CT datasets. Further work is planned to extend the applicability of the methodology to samples of different shapes and dimensions, including industrial parts.

CRediT authorship contribution statement

Bonato Nicolò: Writing – review & editing, Writing – original draft, Visualization, Validation, Software, Methodology, Investigation, Formal analysis, Data curation, Conceptualization. **Zanini Filippo:** Writing – review & editing, Writing – original draft, Visualization, Validation, Resources, Project administration, Methodology, Investigation, Funding acquisition, Data curation, Conceptualization. **Carmignato Simone:** Writing – review & editing, Validation, Supervision, Resources, Project administration, Methodology, Data curation, Conceptualization.

Declaration of Competing Interest

The authors declare that they have no known competing financial interests or personal relationships that could have appeared to influence the work reported in this paper.

Data Availability

Data will be made available on request.

Acknowledgements

The work received funding from DTG – University of Padova, through the research project BIRD 222741/22.

References

[1] M. Schmidt, et al., Laser based additive manufacturing in industry and academia, CIRP Ann. 66 (2) (2017) 561–583, https://doi.org/10.1016/j.cirp.2017.05.011.
[2] H. Gong, et al., Analysis of defect generation in Ti–6Al–4V parts made using powder bed fusion additive manufacturing processes, Addit. Manuf. 1–4 (2014) 87–98, https://doi.org/10.1016/j.addma.2014.08.002.
[3] A. Du Plessis, et al., Effects of defects on mechanical properties in metal additive manufacturing: a review focusing on X-ray tomography insights, Mater. Des. 187 (2020), 108385, https://doi.org/10.1016/j.matdes.2019.108385.
[4] U. Ali, et al., Identification and characterization of spatter particles and their effect on surface roughness, density and mechanical response of 17-4 PH stainless steel laser powder-bed fusion parts, Mater. Sci. Eng.: A 756 (2019) 98–107, https://doi.org/10.1016/j.msea.2019.04.026.
[5] E. Wycisk, et al., Fatigue performance of laser additive manufactured Ti–6Al–4V in very high cycle fatigue regime up to 10^9 cycles, Front. Mater. 2 (2015), https://doi.org/10.3389/fmats.2015.00072.
[6] Z. Snow, et al., Observation of spatter-induced stochastic lack-of-fusion in laser powder bed fusion using in situ process monitoring, Addit. Manuf. 61 (2023), 103298, https://doi.org/10.1016/j.addma.2022.103298.
[7] M. Grasso, et al., In-situ measurement and monitoring methods for metal powder bed fusion: an updated review, Meas. Sci. Technol. 32 (2021), 112001, https://doi.org/10.1088/1361-6501/ac0b6b.
[8] F. Caltanissetta, et al., Characterization of in-situ measurements based on layerwise imaging in laser powder bed fusion, Addit. Manuf. 24 (2018) 183–199, https://doi.org/10.1016/j.addma.2018.09.017.
[9] V. Renken, et al., Development of an adaptive, self-learning control concept for an additive manufacturing process, CIRP J. Manuf. Sci. Technol.,19 (2017) 57–61, https://doi.org/10.1016/j.cirpj.2017.05.002.
[10] S. Coeck, et al., Prediction of lack of fusion porosity in selective laser melting based on melt pool monitoring data, Addit. Manuf. 25 (2019) 347–356, https://doi.org/10.1016/j.addma.2018.11.015.
[11] W. Zouhri, et al., Optical process monitoring for Laser-Powder Bed Fusion (L-PBF), CIRP J. Manuf. Sci. Technol. 31 (2020) 607–617, https://doi.org/10.1016/j.cirpj.2020.09.001.
[12] A. Caggiano, et al., Machine learning-based image processing for on-line defect recognition in additive manufacturing, CIRP Ann. 68 (2019) 451–454, https://doi.org/10.1016/j.cirp.2019.03.021.
[13] M. Grasso, B.M. Colosimo, Process defects and in-situ monitoring methods in metal powder bed fusion: a review, Meas. Sci. Technol. 28 (2017), 044005, https://doi.org/10.1088/1361-6501/aa5c4f.
[14] L. Scime, et al., Layer-wise anomaly detection and classification for powder bed additive manufacturing processes: A machine-agnostic algorithm for real-time

pixel- wise semantic segmentation, Addit. Manuf. 36 (2020), 101453, https://doi.org/10.1016/j.addma.2020.101453.
[15] G. Mohr, et al., In-situ defect detection in laser powder bed fusion by using thermography and optical tomography—comparison to computed tomography, Metals 10 (2020), https://doi.org/10.3390/met10010103.
[16] L. Goossens, B. Van Hooreweder, A virtual sensing approach for monitoring melt-pool dimensions using high speed coaxial imaging during laser powder bed fusion of metals, Addit. Manuf. 40 (2021), 101923, https://doi.org/10.1016/j.addma.2021.
[17] J.B. Forien, et al., Detecting keyhole pore defects and monitoring process signatures during laser powder bed fusion: A correlation between in situ pyrometry and ex situ X-ray radiography, Addit. Manuf. 35 (2020), 101336, https://doi.org/10.1016/j.addma.2020.101336.
[18] J.R. Tempelman, et al., Detection of keyhole pore formations in laser powder-bed fusion using acoustic process monitoring measurements, Addit. Manuf. 55 (2022), 102735, https://doi.org/10.1016/j.addma.2022.102735.
[19] H. Baumgartl, et al., A deep learning-based model for defect detection in laser-powder bed fusion using in-situ thermographic monitoring, Progess Addit. Manuf. 5 (2020) 277–285, https://doi.org/10.1007/s40964-019-00108-3.
[20] Z. Snow, et al., Toward in-situ flaw detection in laser powder bed fusion additive manufacturing through layerwise imagery and machine learning, J. Manuf. Syst. 59 (2021) 12–26, https://doi.org/10.1016/j.jmsy.2021.01.008.
[21] L. Scime, et al., Using machine learning to identify in-situ melt pool signatures indicative of flaw formation in a laser powder bed fusion additive manufacturing process, Addit. Manuf. 25 (2019) 151–165, https://doi.org/10.1016/j.addma.2018.11.010.
[22] Z. Smoqi, et al., Monitoring and prediction of porosity in laser powder bed fusion using physics-informed meltpool signatures and machine learning, J. Mater. Process. Technol. 304 (2022), 117550, https://doi.org/10.1016/j.jmatprotec.2022.117550.
[23] R.K. Leach, et al., Geometrical metrology for metal additive manufacturing, CIRP Ann. 68 (2) (2019) 677–700, https://doi.org/10.1016/j.cirp.2019.05.004.
[24] A. Ulbricht, et al., Can potential defects in PBF-LB/M be healed from the laser exposure of subsequent layers? A quantitative study, Metals 11 (2021), https://doi.org/10.3390/met11071012.
[25] M. Ferrucci, et al., Lessons learned in the design of reference fiducials for layer-wise analysis of test coupons made by laser powder bed fusion, Addit. Manuf. 42 (2021), 101997, https://doi.org/10.1016/j.addma.2021.101997.
[26] S. Oster, et al., On the registration of thermographic in situ monitoring data and computed tomography reference data in the scope of defect prediction in laser powder bed fusion, Metals 12 (6) (2022) 947, https://doi.org/10.3390/met12060947.
[27] Bonato N., et al. (2022). On the alignment of in-process and post-process measurement datasets acquired for precision enhancement of laser powder bed fusion of metals. Euspen 22nd International Conference and Exhibition, Geneva (CH). 2-s2.0–85145581987.
[28] T. Vaneker, et al., Design for additive manufacturing: framework and methodology, CIRP Ann. 69 (2) (2020) 578–599, https://doi.org/10.1016/j.cirp.2020.05.006.
[29] S. Carmignato, et al., Dimensional artefacts to achieve metrological traceability in advanced manufacturing, CIRP Ann. 69 (2) (2020) 693–716, https://doi.org/10.1016/j.cirp.2020.05.009.
[30] A. Charles, et al., Elucidation of dross formation in laser powder bed fusion at down-facing surfaces: Phenomenon-oriented multiphysics simulation and experimental validation, Addit. Manuf. 50 (2022), 102551, https://doi.org/10.1016/j.addma.2021.102551.
[31] E. Eschner, et al., Correlation of spatter behavior and process zone formation in powder bed fusion of metals, CIRP Ann. 69 (1) (2020) 209–212, https://doi.org/10.1016/j.cirp.2020.04.092.
[32] P. Hermanek, et al., Traceable porosity measurements in industrial components using X-ray computed tomography, J. Manuf. Sci. Eng. 141 (2019), 051004, https://doi.org/10.1115/1.4043192.
[33] S. Leuders, et al., Fatigue strength prediction for titanium alloy TiAl6V4 manufactured by selective laser melting, Metall. Mater. Trans. A 46 (2015) 3816–3823, https://doi.org/10.1007/s11661-015-2864-x.
[34] Y.N. Hu, et al., A new approach to correlate the defect population with the fatigue life of selective laser melted Ti-6Al-4V alloy, Int. J. Fatigue 137 (2020), 105584, https://doi.org/10.1016/j.ijfatigue.2020.105584.